

Near-field diffraction of protons by a nanostructured metallic grating under external electric field: Asymmetry and sidebands in Talbot self-imaging

Sushanta Barman* and Sudeep Bhattacharjee†

Department of Physics, Indian Institute of Technology-Kanpur, Kanpur 208016, India

Self-imaging in near-field diffraction is a practical application of coherent manipulation of matter waves in Talbot interferometry. In this work, near-field diffraction of protons by a nanostructured metallic grating under the influence of (a) uniform, (b) spatially modulated, and (c) temporally modulated electric fields are investigated. Time-domain simulations of two-dimensional Gaussian wave packets for protons are performed by solving the time-dependent Schrödinger's equation using the generalized finite difference time domain (GFDTD-Q) method for quantum systems. Effects of strength (E_0) and orientation (θ) of the uniform electric field on the diffraction properties, such as fringe pattern, intensity of the peaks, fringe shift, and visibility, are investigated. The results show that the Talbot fringes shift significantly in the transverse direction even for a small change in the applied electric field ($\Delta E_0 = 0.1$ V/m) and its orientation ($\Delta\theta = 0.1^\circ$). Moreover, electric field-dependent fringe visibility is observed, which can be tuned by E_0 and θ . The potential barriers arising from a spatially modulated electric field are observed to cause significant distortions in the Talbot patterns when the modulation length (λ') is equal to the de Broglie wavelength (λ_{dB}). Sidebands are observed in the Talbot pattern due to the efficient transfer of energy from the oscillating field to the wave packet when the frequency of oscillation (ω) is of the order of $\omega_0 (= 2\pi/T_0)$, where T_0 is the interaction time. This study will be helpful in uniform electric field-controlled precision metrology, developing a highly sensitive electric field sensor based on Talbot interference, and precisely aligning the matter wave optical setup. Furthermore, the sidebands in the Talbot fringe can be used as a precise tool as momentum splitter in matter wave interferometry.

Keywords: Near-field diffraction, Talbot effect, wave packets, nanostructured grating, matter wave interferometry

I. INTRODUCTION

In near-field diffraction of a plane wave, the diffraction grating creates self-images at regular distances away from it. This phenomenon was observed in classical optics in 1836 by Henry Fox Talbot [1] and is known as the Talbot effect [2–6]. Since the discovery, the Talbot effect has been used in many optical applications ranging from surface profiling of transparent objects [7] and testing of beam collimation [8] to several precision measurements, such as vibration in real-time [9], periodic phase modulation [10], aberration [11], focal dimension of lenses [12], small tilt angle [13], grating parameters [14], and temperature profile of gaseous flame [15]. Recently, this effect was used to detect optical vortices [16] and the construction of high-resolution spectrometers [17].

Due to the wave nature, quantum particles also show diffraction effects, which are similar to those in the case of light. After the first observation of wave nature for electron [18], several experiments were performed on matter wave diffraction to study the quantum effects [19–24], which resulted in the development of matter wave interferometers. Similar to classical optics, the Talbot effect was observed experimentally in matter wave optics for electron [25], positron [26], neutral atoms [27–30], and complex molecules [31–38].

Recently, there has been a huge surge in research on quantum technologies for computing, materials, communication, and instrumentation. These efforts drive the formulation of novel concepts and the development of quantum devices, such as sensors and circuitry for quantum memories. In this regard,

the near-field diffraction of matter waves has become an important tool for studying quantum effects and measurement of fundamental quantities. Therefore, there is a need to understand the phenomenon under different conditions. Several theoretical as well as experimental investigations have been carried out in this direction. The Talbot effect in the near-field diffraction was studied by solving Fresnel-Kirchhoff integral in paraxial approximation for a three-grating setup with uncollimated incident particles [39]. Interference pattern formation in Talbot-Lau interferometers was studied by combining semiclassical scattering theory with a phase space formulation accounting for arbitrary grating interactions and realistic beam properties [40]. The same phenomenon has been studied for large molecules by considering the reconstruction of the Wigner distribution function (WDF), where the experimental conditions of the WDF reconstruction have been estimated for the Talbot interference fringes [41]. The diffraction of cold Rb atoms by a single-, double-, and multiple-slit grating were studied in the near-field to the far-field region, including the transition region, using the Feynman path integration method [42, 43]. Another theoretical study discussed the possibility of Talbot self-imaging for relativistic matter waves [44].

Apart from these theoretical studies, numerous experimental studies have been performed in parallel. Three equally spaced transmission gratings were employed to study the transition from the classical description of the diffraction pattern with Xe atoms to the Talbot-Lau interference in the quantum regime with H atoms [30]. Furthermore, the feasibility of interferometers based on charged particles, such as protons and antiprotons, have been discussed. The matter wave interference of positrons in a Talbot-Lau interferometer was demonstrated [26]. Experiments have been performed on the near-field diffraction for atoms, such as He [27], Na [28], and Cs [29]. Scalar polarizabilities of complex molecules, such as

* sushanta@iitk.ac.in

† sudeepb@iitk.ac.in

C_{60} , C_{70} [32, 33, 35], $C_{30}H_{12}F_{30}N_2O_4$ [34], $C_{49}H_{16}F_{52}$ [36] and silicon nanoparticle [37], were measured using the near-field matter wave interferometry.

Numerical studies have also been performed to study ultrafast revivals of quantum states associated with the temporal Talbot effect, which results in higher-order harmonic generation and suggests developing subnanometer ultrafast Talbot interferometers [45]. Kazemi et al. have performed numerical investigations on the effect of decoherence on Talbot images [46]. Studies on near-field diffraction of charged or neutral antimatter particles suggest that the van der Waals interactions for the polarizable particle are critical to the fringe visibility [47].

Studies so far suggest that the Talbot effect in near-field diffraction is not only an interesting matter wave phenomenon but also leads to the various applications mentioned above. However until now, there are no studies on the effect of external electric fields on the near-field diffraction of charged particles, such as protons, and how the electric fields control the Talbot pattern, including their potential applications.

In this study, near-field diffraction of protons by a nanostructured metallic grating in the presence of (a) uniform, (b) spatially modulated, and (c) temporally modulated electric fields are investigated. Time-domain simulations are performed using the generalized finite difference time domain (GFDTD-Q) method for quantum systems to simulate two-dimensional Gaussian wave packets of protons. The effect of the applied uniform electric field strength (E_0) and its orientation (θ) on the Talbot pattern are investigated. The diffracted wave packet is analyzed in the wave number space (k_x, k_y) to investigate the quantization of axial (k_x) and lateral (k_y) wave numbers. The results show that the fringe pattern gets shifted in the transverse direction. Moreover, it is found that E_0 and θ can tune the fringe shift and visibility. Distortions are observed in the Talbot fringe in the case of spatially modulated electric field when the modulation length (λ') is equal to the de Broglie wavelength (λ_{dB}). Due to the efficient energy transfer from the oscillating field to the wave packet, multiple sidebands are observed for the first time in the Talbot pattern when the oscillation frequency (ω) is of the order of $\omega_0 (= 2\pi/T_0)$ with T_0 being the interaction time. Being a lighter ion, a proton responds easily, even to a small electric field. The findings of this research have important implications in electric field-controlled precision metrology, to develop a highly sensitive electric field sensor based on the Talbot effect and in precise alignment of matter wave optical setup. Furthermore, the sidebands observed in the Talbot fringe will be useful as momentum splitters in matter wave interferometry.

The article is structured as follows. Section II describes the numerical method for time-domain simulation of matter waves. In Sec. III, wave packet simulation results are presented and discussed. Finally, conclusions are made in Sec. IV.

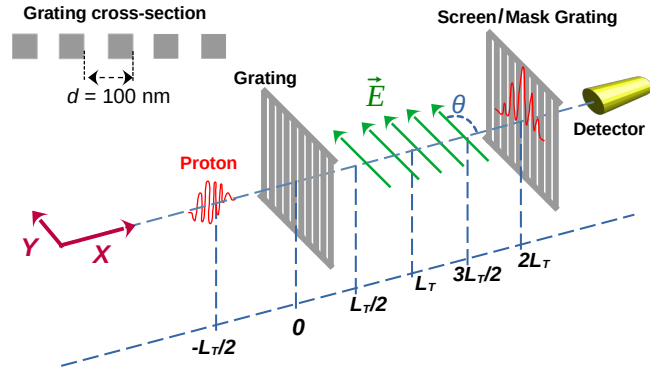


FIG. 1. Schematic diagram of the diffraction setup under investigation. A metallic grating having periodicity $d = 100$ nm and opening fraction $f = 50\%$ is used to diffract protons. The incident particles move along the $+x$ direction with an initial velocity $v = 394$ m/s. Similar to the diffraction grating, a mask grating is placed at $x = 2L_T$, where $L_T (= d^2/\lambda_{dB})$ is the Talbot length with λ_{dB} being the de Broglie wavelength of protons. An electric field (\vec{E}) is applied in the region $L_T/2 \leq x \leq 3L_T/2$ behind the diffraction grating. The electric field \vec{E} makes an angle θ with the x -axis. A detector is placed behind the mask grating to detect the diffracted particles at various positions along the y -axis.

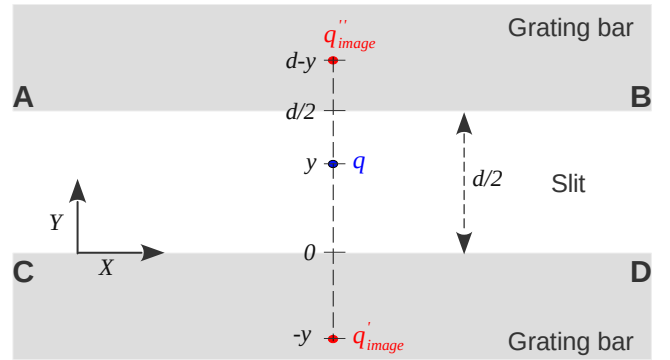


FIG. 2. A cross-sectional view of the diffraction grating. ABCD is one of the slit openings in the grating. AB and CD are the planes of two neighboring bars of the grating. Since the grating is made of metal, image charges (q'_{image} and q''_{image}) are induced due to a charge q situated at a distance y from the lower plane (CD). The width of the slit is $d/2$.

II. METHOD

The setup for Talbot-Lau interferometer consists of three gratings, where the first grating is used to make a coherent source of matter waves [48, 49]. The diffraction of coherent waves occurs in the second grating, while the third grating acts as a mask grating. Thus, self-imaging by the second grating can be considered for a complete description of the diffraction phenomenon in the interferometer [39]. The setup under consideration consists of a metallic grating having periodicity $d = 100$ nm and opening function $f = 50\%$, as shown in Fig. 1. The first grating is absent as we consider incident monoenergetic and coherent protons that move

along the x -direction with a velocity $v = 394$ m/s. The corresponding de Broglie wavelength $\lambda_{dB} = 1$ nm and kinetic energy $E_{k0} = 0.813$ meV. The ion beams are extracted from a cryo-plasma [50, 51], and then, the beams are collimated to the required energy, in an experiment that is currently under development in our laboratory. Usually, these experiments are performed in high vacuum ($< 10^{-7}$ mbar) to minimize dissipation through ion-atoms collisions. The image of the diffraction grating repeats at the Talbot length $L_T = d^2/\lambda_{dB}$ [52]. An electric field (\vec{E}) is applied in the region $L_T/2 \leq x \leq 3L_T/2$, as shown in Fig. 1. The diffraction phenomena of protons can be investigated by solving the two-dimensional (x, y) time-dependent Schrödinger's equation given by

$$i\hbar \frac{\partial \psi(x, y, t)}{\partial t} = \left[-\frac{\hbar^2}{2m} \nabla^2 + V_g(x, y) + eV_{image}(x, y) + eV_E(x, y, t) \right] \psi(x, y, t), \quad (1)$$

where $i = \sqrt{-1}$, and $\psi(x, y, t)$, m , e , and \hbar are the wavefunction, mass of proton, electronic charge, and reduced Planck's constant, respectively. $V_g(x, y)$ is the geometric potential considering the grating bars as hard walls [53, 54]. $V_{image}(x, y)$ is the electrostatic potential due to the induced image charge in the conducting bars of the grating, and $V_E(x, y, t)$ is the electrostatic potential due to the applied electric field \vec{E} .

The geometric potential of a periodic grating can be expressed as [55, 56],

$$V_g(x, y) = V_{g0} \begin{cases} \sum_{m=-\infty}^{+\infty} \Pi\left(\frac{y-md}{d/2}\right), & \text{if } 0 \leq x \leq l \text{ and all } y \\ 0, & \text{if otherwise} \end{cases} \quad (2)$$

where l and V_{g0} are the grating thickness and height of the geometrical potential barrier, respectively. The cross-section of the grating bars are assumed to be rectangular, as shown in Fig. 1. The value of V_{g0} is taken as $\sim 30E_{k0}$, which is well above the incident particle energy, to minimize the effect of quantum tunneling through the grating bars [40, 57]. The $\Pi(u)$ function is the unit impulse function, which is given by,

$$\Pi(u) = \begin{cases} 0, & \text{if } |u| > 1/2 \\ 1, & \text{if } |u| < 1/2 \\ \frac{1}{2}, & \text{if } |u| = 1/2 \end{cases} \quad (3)$$

When a proton passes through the slits, it interacts with the walls of the grating bars. The proton-wall interaction can be described by the image charge potential, which can be obtained from the well-known image charge solution of Laplace's equation by treating the slit walls as infinite planes. This method has also been used to evaluate particle-grating interactions in previous studies of electron diffraction [58]. Considering the grating walls as infinite planes, as shown in

Fig. 2, the image charge potential is obtained as [58]

$$V_{image}(x, y) = \frac{e}{8\pi\epsilon_0} \left[\frac{q'_{image}}{y} + \frac{q''_{image}}{(d/2-y)} \right], \text{ if } 0 < y < d/2 \text{ and } 0 \leq x \leq l \quad (4)$$

where ϵ_0 is the electric permittivity of free space. For metal grating, the induced image charges can be obtained as $q'_{image} = q''_{image} = -e$.

Before starting the numerical calculations, Eq. (1) is nondimensionalized in arbitrary units of space and time to make it computationally advantageous. The spatial and temporal domains are transformed as $\vec{r}(x, y) = \gamma\vec{R}(X, Y)$ and $t = \tau T$, respectively. Where γ and τ have the dimension of length (m) and time (s), respectively. Therefore, the 2D Laplacian in the new coordinate system can be expressed as $\nabla^2 = (1/\gamma^2)\nabla_\gamma^2 = (1/\gamma^2)(\partial^2/\partial X^2 + \partial^2/\partial Y^2)$. Similarly, the potential energies are scaled as $\phi_g(X, Y) = (1/V_0)V_g(x, y)$, $\phi_{image}(X, Y) = (e/V_0)V_{image}(x, y)$, and $\phi_E(X, Y, T) = (e/V_0)V_E(x, y, t)$ with the scaling factor $V_0 = \hbar^2/2m\gamma^2$, which has a dimension of energy. The functions $\phi_g(X, Y)$, $\phi_{image}(X, Y)$, and $\phi_E(X, Y, T)$ are dimensionless functions. Thereafter, the nondimensionalized form of Eq. (1) is obtained by taking $\gamma = \sqrt{\hbar^2/2mV_0}$ and $\tau = 2m\gamma^2/\hbar$, as

$$i \frac{\partial \psi(R, T)}{\partial T} = \left[-\nabla_\gamma^2 + \phi_g(R) + \phi_{image}(R) + \phi_E(R, T) \right] \psi(R, T), \quad (5)$$

where the wavefunction $\psi(R, T)$ can be separated into real ($\psi_{real}(R, T)$) and imaginary ($\psi_{imag}(R, T)$) parts as $\psi(R, T) = \psi_{real}(R, T) + i\psi_{imag}(R, T)$.

The real and imaginary parts of Eq. (5) are equated, and the following coupled equations are obtained,

$$\frac{\partial \psi_{real}(R, T)}{\partial T} = \left[-\nabla_\gamma^2 + \phi_g(R) + \phi_{image}(R) + \phi_E(R, T) \right] \psi_{imag}(R, T), \quad (6)$$

and

$$\frac{\partial \psi_{imag}(R, T)}{\partial T} = \left[\nabla_\gamma^2 - \phi_g(R) - \phi_{image}(R) - \phi_E(R, T) \right] \psi_{real}(R, T). \quad (7)$$

The coupled Eqs. (6) and (7) are solved using generalized finite difference time domain (GFDTD-Q) method [59] for quantum mechanics to obtain the time evolution of an initial wave function $\psi(X, Y, T = 0)$. The time evolution of $\psi_{real}(X, Y, T)$ and $\psi_{imag}(X, Y, T)$ is obtained using the leapfrog method.

The GFDTD-Q method is a powerful numerical tool for an explicit solution of linear and nonlinear time-dependent

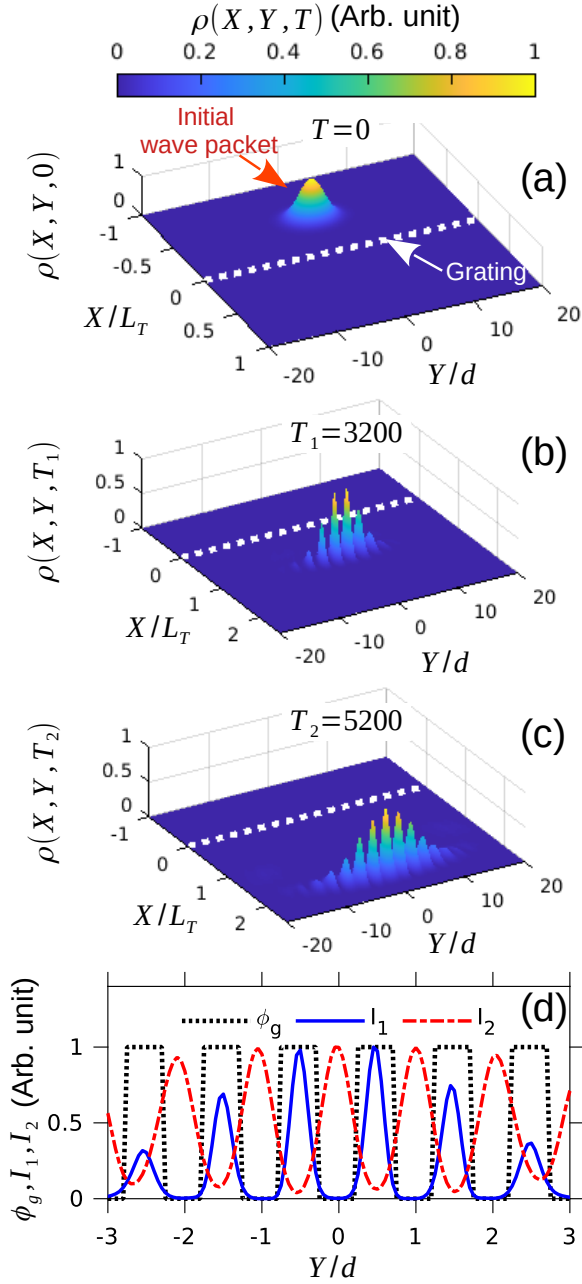


FIG. 3. (a) Distribution of the probability density ($\rho(X, Y, 0) = |\psi(X, Y, 0)|^2$) of the initial Gaussian wave packet moving along the $+x$ direction. Distribution of the probability density ($\rho(X, Y, T) = |\psi(X, Y, T)|^2$) of the diffracted wave packet at (b) $T_1 = 3200$ and (c) $T_2 = 5200$, when the wave packet reached at $X_1 = L_T$ and $X_2 = 2L_T$, respectively. (d) Comparison of the intensities in the diffraction patterns, $I_1 = |\psi(L_T, Y, T_1)|^2$ and $I_2 = |\psi(2L_T, Y, T_2)|^2$ with the grating function ($\phi_g(0, Y)$).

Schrödinger's equations, which appear in various physical systems [60–63]. In this method, the temporal and spatial differential operators are approximated as centered difference equations. The scheme is stable and accurate up to $(\Delta T)^3$ and $(\Delta X)^5$. A complete study on the stability analysis of this method may be found in Ref. [59, 61]. Physical systems hav-

ing potentials of any arbitrary configuration can be simulated using the GFDTD-Q method [64–73]. Moreover, this method has already been applied in previous studies to simulate matter wave diffraction phenomena [54, 57]. A detailed formulation of the GFDTD-Q method and the numerical procedures can be found in Ref. [54].

The initial wave packet is taken as a two-dimensional Gaussian wave packet given by

$$\psi(X, Y, T = 0) = C \exp \left[-\frac{1}{2} \left\{ \frac{(X - X_0)^2}{\sigma_X^2} + \frac{(Y - Y_0)^2}{\sigma_Y^2} \right\} + ik(X - X_0) \right], \quad (8)$$

where C is the normalization constant and (X_0, Y_0) is the center of the wave packet at $T = 0$. σ_X and σ_Y are the width of the wave packet along X and Y -axes, respectively. k ($= 2\pi/\lambda_{dB}$) is the wave number of the wave packet.

A 2D region of 501×501 square grids ($\Delta X = \Delta Y$) has been considered in the simulation. The spatial and temporal scaling factors are taken as $\gamma = 2.5 \text{ \AA}$ and $\tau = 1.982 \times 10^{-12} \text{ s}$. The details of the simulation parameters are listed in Table I. The convergence in the simulation is confirmed by checking the unit norm of the initial wave packet $\psi(X, Y, T = 0)$ at each time step.

In the simulations, artificial reflections occur when the wave packet hits the boundary of the numerical box. Hence, absorptive boundary conditions are employed to avoid such unwanted reflections from the boundaries. At each time step, the wave function is multiplied by a damping function $\zeta(X)$ given by [74]

$$\zeta(X) = \frac{1}{1 + \exp\left(-\frac{X - X_0}{\Lambda}\right)}, \quad (9)$$

where Λ ($= 5$) and X_0 ($= 0$) are two parameters that determine the sharpness and position of the damping function for the left boundary. The $\zeta(X)$ function has a unit value for all X except near the boundary where the wave function needs to be suppressed to minimize artificial reflections. The corresponding damping function for the right boundary is obtained by choosing the proper values of X_0 ($= X_{max}$) and Λ ($= -5$). Similar damping functions have been implemented in the simulation for the upper and lower boundaries.

The wave packet in the wave number space (k_x, k_y) can be obtained by Fourier transformation as

$$\psi_k(k_x, k_y, t) = \frac{1}{2\pi} \int \int \psi(x, y, t) e^{-i(k_x x + k_y y)} dx dy. \quad (10)$$

III. RESULTS AND DISCUSSIONS

A. Near-field diffraction without electric field

Fig. 3 (a) shows the distribution of the initial wave packet $\rho(X, Y, T = 0)$. The wave packet evolves with time and gets

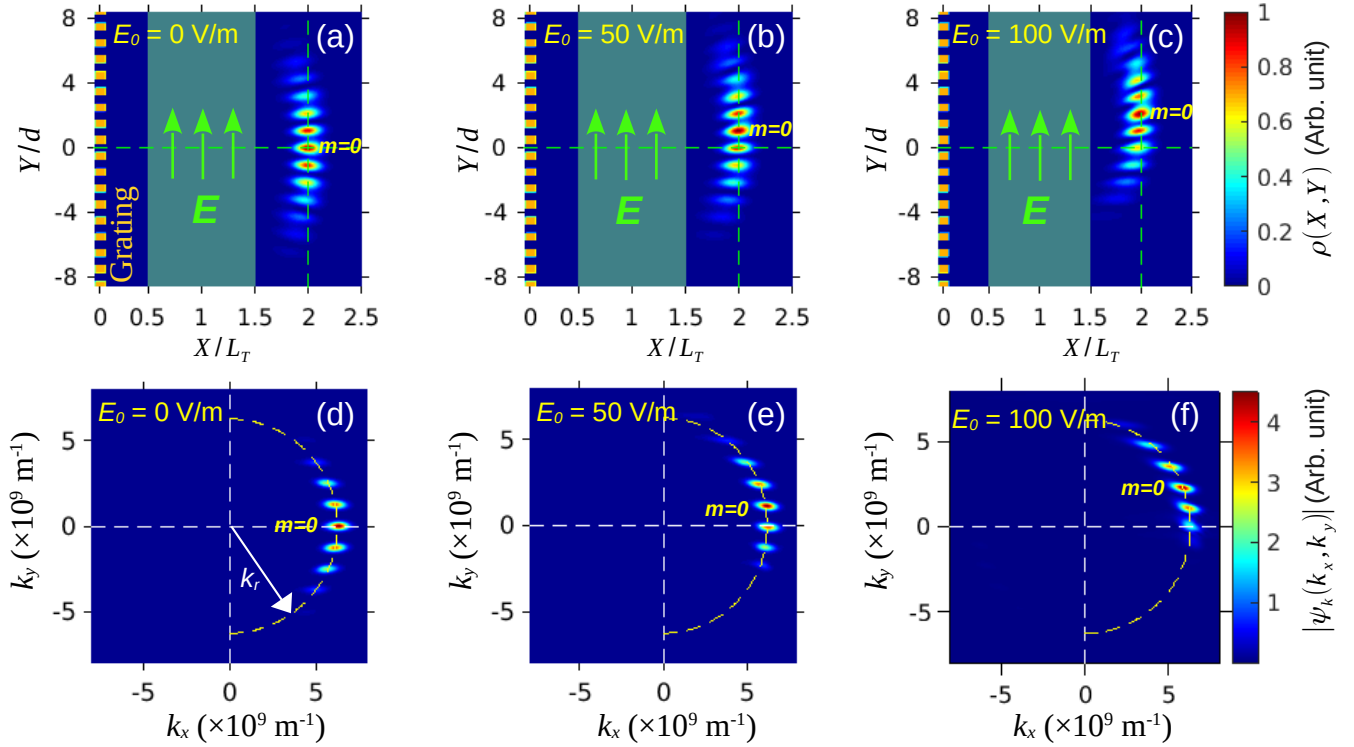


FIG. 4. Final shape of the diffracted wave packet at $T_2 = 5200$: the panels (a)-(c) are shown in position space (X, Y) , and panels (d)-(f) are shown in wave number space (k_x, k_y) . The panels (a) and (d) are plotted for the magnitude of the applied electric field $E_0 = 0$ V/m; (b) and (e) are plotted at $E_0 = 50$ V/m; (c) and (f) are plotted at $E_0 = 100$ V/m. In all the cases, the electric field is applied in the transverse direction ($\theta = 90^\circ$) to the direction of incidence (x -axis) of the particle.

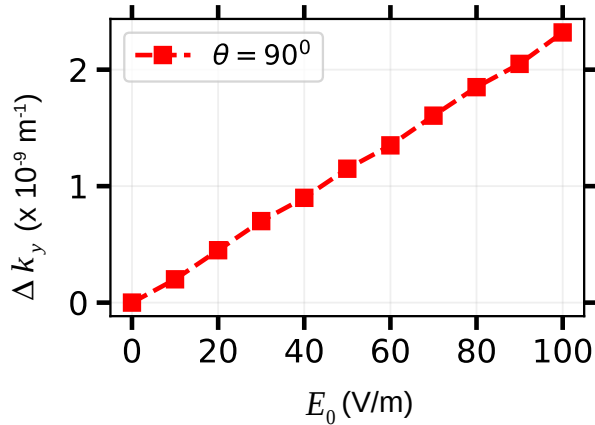


FIG. 5. Variation of the change in transverse wave number Δk_y of the diffracted wave packet with the applied uniform electric field strength E_0 . The values of Δk_y are obtained at $X_2 = 2L_T$ for the orientation of the electric field $\theta = 90^\circ$.

diffracted by the grating. The distribution of the probability density of the wave packet behind the diffraction grating at time $T_1 = 3200$ and $T_2 = 5200$ are shown in Figs. 3 (b) and (c), respectively. It can be noticed that at T_1 and T_2 , the diffracted wave packet reached at $X_1 = L_T$ and $X_2 = 2L_T$, respectively.

TABLE I. Values of the parameters used in the simulation.

Parameters	Values
σ_x	50 nm
σ_y	250 nm
(X_0, Y_0)	$(-L_T/2, 0)$
de Broglie Wavelength (λ_{dB})	1 nm
Velocity of the incident proton (v)	394 m/s
Periodicity of the grating (d)	100 nm
Opening function of the grating (f)	50%
Thickness of the grating (l)	50 nm
Geometrical potential barrier height (V_{g0})	24.390 meV
V_0	0.332 meV
γ	2.5 Å
τ	1.982×10^{-12} s
Magnitude of the electric field (E_0)	0 – 100 V/m
Orientation of the electric field (θ)	$0^\circ - 90^\circ$

At later times (T_2), higher order peaks ($m = \pm 6$) are observed (see Fig. 3 (c)), which are not observed at T_1 (maximum order $m = \pm 4$) (see Fig. 3 (b)). This happens because in the near-field regime, the shape of the diffracted wave packet evolves with time, and there exists a time delay between the central maxima and the higher order peaks, as reported in an earlier investigation [54]. Furthermore, from the distribution of diffracted wave packets at $T_1 = 3200$ and $T_2 = 5200$, it is clear

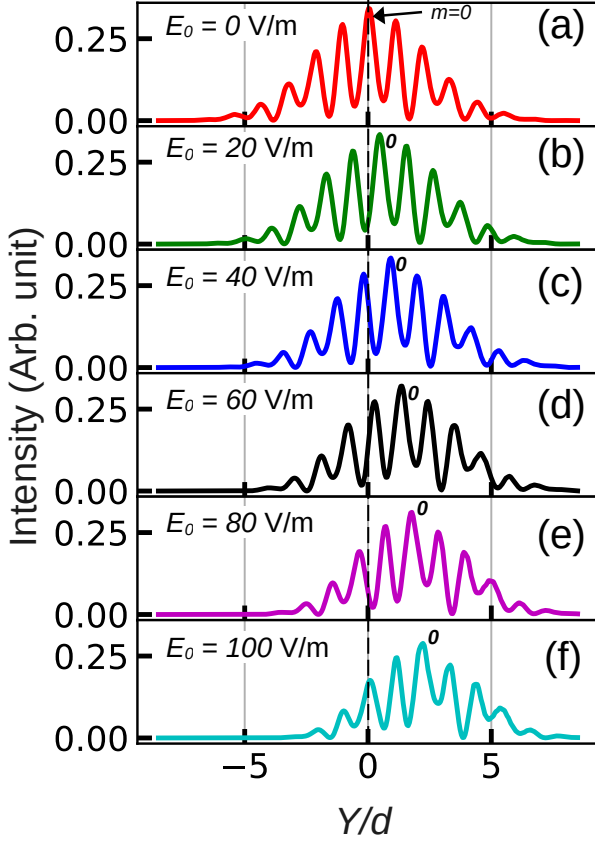


FIG. 6. Fringe pattern at $X_2 = 2L_T$ for different magnitudes (E_0) of the applied electric fields in the transverse direction ($\theta = 90^\circ$). (a) $E_0 = 0$ V/m, (b) $E_0 = 20$ V/m, (c) $E_0 = 40$ V/m, (d) $E_0 = 60$ V/m, (e) $E_0 = 80$ V/m, and (f) $E_0 = 100$ V/m.

that the fringe periodicity becomes equal to the grating periodicity (d). This phenomenon is known as the Talbot effect, which is distinct from the far-field diffraction, where the probability density peaks at an angle $\alpha = \sin^{-1}(m\lambda_{dB}/d)$ behind the diffraction grating [75].

For further understanding of the diffraction properties, the intensities of the fringe pattern on a screen placed at $X_1 = L_T$ and $X_2 = 2L_T$ are obtained as $I_1 = |\psi(L_T, Y, T_1)|^2$ and $I_2 = |\psi(2L_T, Y, T_2)|^2$, respectively. The variation of I_1 , I_2 , and the grating function $\phi_g(0, Y)$ along the transverse direction (Y) are shown Fig. 3 (d). The figure shows that both I_1 and I_2 vary sinusoidally with a decaying amplitude on either side from the center ($Y = 0$) of the grating. Moreover, I_1 varies with 180° out of phase to the grating function, whereas I_2 varies with the same phase as $\phi_g(0, Y)$. These characteristics of Talbot patterns, which are observed in earlier studies as well [75], confirm the accuracy of the simulation techniques used in this study.

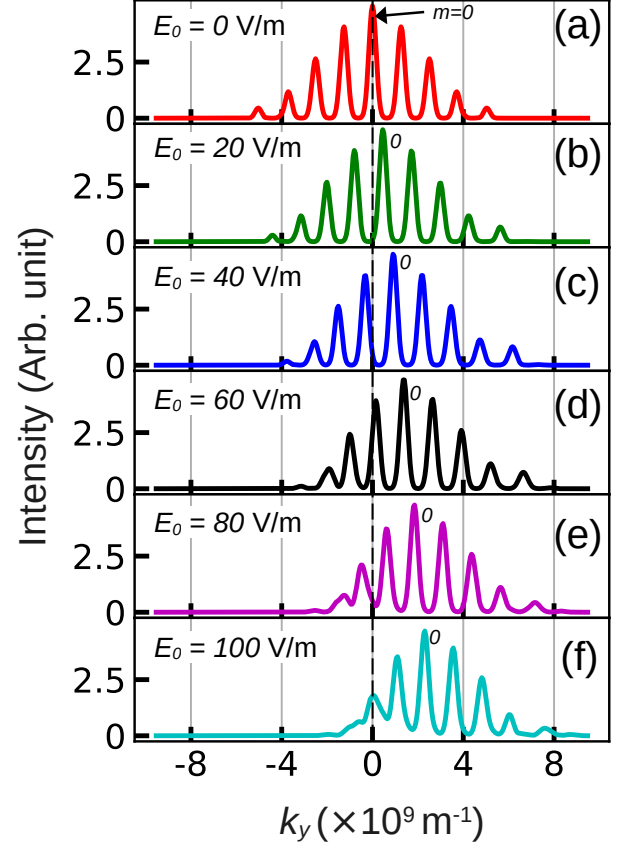


FIG. 7. Fringe pattern in the momentum space (k_x, k_y) for different magnitudes of electric fields (a) $E_0 = 0$ V/m, (b) $E_0 = 20$ V/m, (c) $E_0 = 40$ V/m, (d) $E_0 = 60$ V/m, (e) $E_0 = 80$ V/m, and (f) $E_0 = 100$ V/m. The electric field is applied in the transverse direction ($\theta = 90^\circ$).

B. Near-field diffraction in a uniform electric field

In this section, we have investigated the time evolution of the diffracted wave packet in the near-field region under the influence of uniform electric fields given by

$$\vec{E}(x, y) = E_0(\hat{x} \cos \theta + \hat{y} \sin \theta), \quad (11)$$

where E_0 and θ are the magnitude of \vec{E} and the angle made by \vec{E} with x -axis, respectively. The electric field is employed in the region $L_T/2 \leq x \leq 3L_T/2$.

The corresponding distribution of the electrostatic potential is obtained as

$$V_E(x, y) = \begin{cases} -E_0(x \cos \theta + y \sin \theta), & \text{if } L_T/2 \leq x \leq 3L_T/2 \\ & \text{and all } y \\ 0, & \text{if otherwise} \end{cases}$$

The effect of the magnitude (E_0) and orientation (θ) of the applied electric field \vec{E} on the diffraction patterns, fringe shift,

and visibility are investigated. Further, the wave packets are analyzed in the wave number space (k_x, k_y) to investigate its transverse quantization after diffraction.

1. Diffraction pattern

Fig. 4(a)-(c) shows the distribution of $\rho(X, Y, T)$ of the diffracted wave packet at time $T_2 = 5200$ for different values of E_0 ($= 0, 50$ and 100 V/m). In all the cases, the electric fields are applied in the transverse direction ($\theta = 90^\circ$). A well-formed pattern is observed for $E_0 = 0$ V/m, as shown in Fig. 4(a). Figs. 4(b) and (c) show that the fringe patterns get shifted along $+y$ -direction and the amount of fringe shift increases with increase in E_0 . The fringe shifts are calculated to be, $s = 1.1 \times d$ and $2.15 \times d$ ($d = 100$ nm) for $E_0 = 50$ and 100 V/m, respectively. Moreover, for large electric fields, higher order peaks ($m \geq +3$) get overlapped with each other, as observed in Fig. 4(c).

Next, the diffracted wave packets are analyzed in the wave number space (k_x, k_y), which are obtained using Eq. (10). Figs. 4(d)-(f) show the distribution of $|\psi_k(k_x, k_y, T)|$ for different values of E_0 ($= 0, 50$ and 100 V/m) at $\theta = 90^\circ$ and $T_2 = 5200$. A semi-circular distribution having radius of $k_r = \sqrt{k_x^2 + k_y^2}$ is observed among the the diffraction peaks in $|\psi(k_x, k_y, T)|$. It is seen that the value of k_r is equal to the wave number of the initial wave packet, $k_0 = 2\pi/\lambda_{dB} = 6.28 \times 10^{-9}$ m $^{-1}$. More interestingly, it is observed that k_r remains constant irrespective of E_0 because the electric field is applied in a direction perpendicular to the motion of the particle. Therefore, no work is done by \vec{E} on the particle, and the momentum remains conserved. However, the diffracted wave packet gets deflected in the perpendicular direction ($+y$ -axis). Hence, the transverse wave number k_y increases with the increase in E_0 while keeping k_r a constant. The change in transverse wave number (Δk_y) with E_0 for $\theta = 90^\circ$ is shown in Fig. 5.

The fringe patterns on a screen placed at $X_2 = 2L_T$ are shown in Figs. 6(a)-(f) for different values of E_0 when the field is applied in the transverse direction ($\theta = 90^\circ$). From Figs. 6(a)-(f), it is clear that the periodicity in the fringe patterns, which is same as the grating periodicity d , remains constant in all the cases. Moreover, all the peaks in the diffraction pattern get shifted equally, and this shift increases with the increase in E_0 . Further, it can be noticed that at large electric fields ($E_0 \geq 80$ V/m), the visibility of the higher order diffraction peaks ($m \geq +3$) get reduced, as shown in Fig. 6(f). A similar trend is observed in the diffraction pattern obtained in the momentum space as shown in Fig. 7(a)-(f). The amplitude of the higher order peaks ($m \geq +3$) decreases at large electric fields (see Fig. 7(f)), which is also clear from Fig. 4(f).

2. Fringe shift

Being a charged particle, the diffracted wave packet of a proton gets shifted along the transverse direction in the presence of \vec{E} . The variation of the fringe shift (s) with E_0 and θ

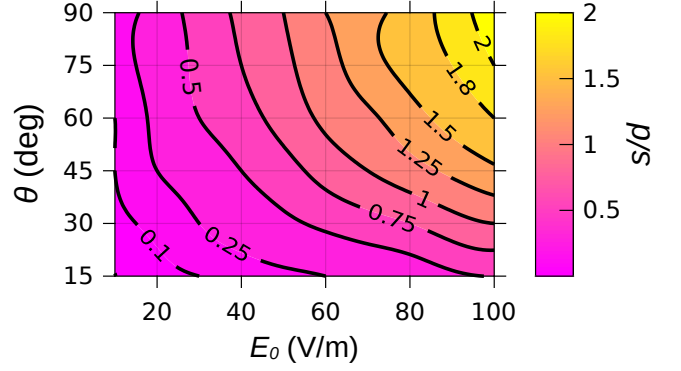


FIG. 8. Variation of fringe shift normalized by the grating period (s/d) with the magnitude E_0 and orientation (θ) of the applied uniform electric field.

is shown in Fig. 8. It is observed that the value of s depends upon both E_0 and θ . Moreover, Fig. 8 shows that s increases when the electric field is applied in the transverse direction. A maximum shift of $s = 2.15 \times d$ is obtained for $E_0 = 100$ V/m and $\theta = 90^\circ$. Furthermore, similar fringe shifts are observed for different combinations of E_0 and θ , which is clear from the contour lines as shown in Fig. 8. This is because the transverse component of the electric field (E_Y) that controls the fringe shift, depends upon both E_0 and θ , which can be evaluated by $E_Y = E_0 \sin \theta$. Next, the sensitivity of the Talbot fringes on E_0 and θ are investigated.

At first, a mask grating with the same opening function ($f = 50\%$) as the diffraction grating is placed at the position of the screen ($X_2 = 2L_T$) as shown in Fig. 1. After that, the mask grating is translated along the y -axis at in steps of $\Delta y = 5$ nm, which can be achieved using commercially available electromagnetically actuated nano-positioning stage [76]. The probability of finding the particle behind the mask grating is evaluated by $I_c = \int_{Y=-\infty}^{+\infty} \int_{X=2L_T}^{\infty} |\psi(X, Y, T)|^2 dX dY$. The variation of the collected intensity (I_c) with the displacement of the mask grating (s_d) for different field strengths at $\theta = 90^\circ$ is shown in Fig. 9(a). The figure shows a sinusoidal variation of the intensity with s_d , as observed in earlier studies for nanoparticles, such as C_{60} , C_{60} [33], and massive particles, such as fluoros porphyrin having a molecular weight of 10123 amu [38]. Initially, at $s_d/d = 0$, the mask grating is placed 180° out of phase to the diffraction grating, and a minimum intensity of $I_c = 19.9\%$ is observed for $E_0 = 0$ V/m, as shown in Fig. 9(a). Thereafter, I_c increases with the displacement of the mask grating for $E_0 = 0$ V/m, and it becomes maximum (32.4%) at $s_d/d = 0.5$ (black dotted line LM) when both the gratings are in phase, and therefore, maximum transmission occurs, as seen in Fig. 9(a). Furthermore, it can be noticed that the values of the collected intensity (I_c) $_{s_d/d=0.5}$, decreases with the increase in E_0 from 0 to 10 V/m due to the fringe shift. Fig. 9(b) shows the variation of (I_c) $_{s_d/d=0.5}$ with the change in electric field strength (ΔE_0), where (I_c) $_{s_d/d=0.5}$ decreases with ΔE_0 . To quantify the dependency of (I_c) $_{s_d/d=0.5}$ upon E_0 , a sensitivity factor is defined as $(SF)_{E_0} = (\Delta I_c / \Delta E_0) \times 100$, and its variation with ΔE_0 is

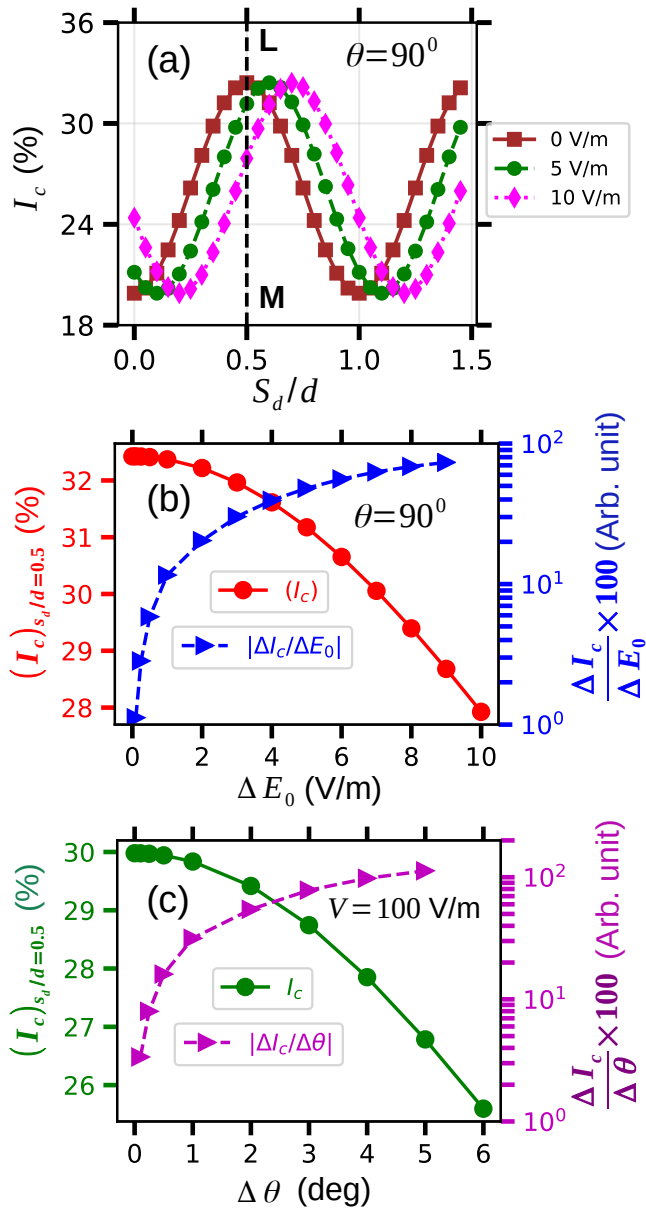


FIG. 9. (a) Variation of the intensity (I_c) collected by the detector behind the mask grating with the displacement of that grating (s_d/d) for different field strengths E_0 (0 – 10 V/m) at a fixed angle $\theta = 90^\circ$. The dashed black line (LM) at $s_d/d = 0.5$, where I_c for $E_0 = 0$ V/m attains a peak, suggests that both diffraction and mask grating are in phase. (b) Variation of the intensity $(I_c)_{s_d/d=0.5}$ collected at $s_d/d = 0.5$ (left y-axis) and its sensitivity to the electric field $(\Delta I_c / \Delta E_0) \times 100$ (right y-axis) with ΔE_0 . (c) Variation of the intensity $(I_c)_{s_d/d=0.5}$ (left y-axis) and its sensitivity to the electric field orientation $(\Delta I_c / \Delta \theta) \times 100$ (right y-axis) with $\Delta \theta$.

shown in Fig. 9(b) (right y-axis). It is found that the field sensitivity factor has a value of $(SF)_{E_0} = 1.1\%$, even for small change in the electric field $\Delta E_0 = 0.1$ V/m, which increases to 73.5% for $\Delta E_0 = 10$ V/m, as shown in Fig. 9(b). Therefore, I_c strongly depends on E_0 , which can be further increased by extending the interaction region beyond L_T (see Fig. 1), as

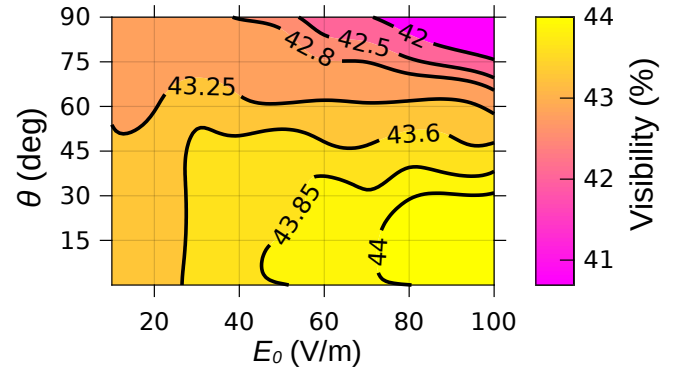


FIG. 10. Variation of the fringe visibility (V) as a function of magnitude E_0 and orientation (θ) of the applied uniform electric field.

used in this study. The electric field sensitivity of the Talbot fringe can be used to detect small electric fields.

A similar variation of I_c with s_d is obtained for different orientations (θ) of \vec{E} (not shown). The variation of $(I_c)_{s_d/d=0.5}$ with $\Delta \theta$ for $E_0 = 100$ V/m is shown in Fig. 9(c) (left y-axis), where $(I_c)_{s_d/d=0.5}$ decreases with the increase in $\Delta \theta$ due to the increase in fringe shift. Fig. 9(c) shows variation of θ sensitivity factor $(SF)_\theta = (\Delta I_c / \Delta \theta) \times 100$ with $\Delta \theta$. The figure shows that $(SF)_\theta$ increases from 3.37% to 112.79% while $\Delta \theta$ is increased from 0.1° to 5° . Therefore, the Talbot fringe is highly sensitive to the orientation of the applied electric field. Furthermore, $(SF)_\theta$ can be enhanced by extending the electric field interaction region beyond $L_T/2 \leq x \leq 3L_T/2$.

3. Fringe visibility

The visibility of a diffraction pattern is an important parameter that determines the resolution of the maxima and minima in the fringe. The fringe visibility (V) is determined by [30]

$$V = \frac{I_{max} - I_{min}}{I_{max} + I_{min}}, \quad (12)$$

where I_{max} and I_{min} are the maximal and minimal intensity in the diffraction pattern.

Fig. 10 shows the variation of fringe visibility with E_0 and θ at $X_2 = 2L_T$. It is observed that V depends upon both E_0 and θ . Further, it varies from 40.8% to 44% in the parameter range used in this numerical investigation. A similar value of V ($\sim 40\%$) has been reported for hydrogen beam diffraction in an earlier experimental study [30]. Here, a maximum visibility (44%) is observed at $E_0 = 100$ V/m and $\theta = 0^\circ$. However, it is seen that the visibility decreases with the increase in E_0 when the field is applied in the transverse direction ($\theta = 90^\circ$), as shown in Fig. 10. This is because a strong electric field in the transverse direction destroys the transverse coherence of the wave packet, which is critical to matter wave diffraction. Therefore, the visibility of the fringe pattern decreases with the increase in E_0 at $\theta = 90^\circ$. On the other hand, the visibility gets enhanced for strong electric field applied along

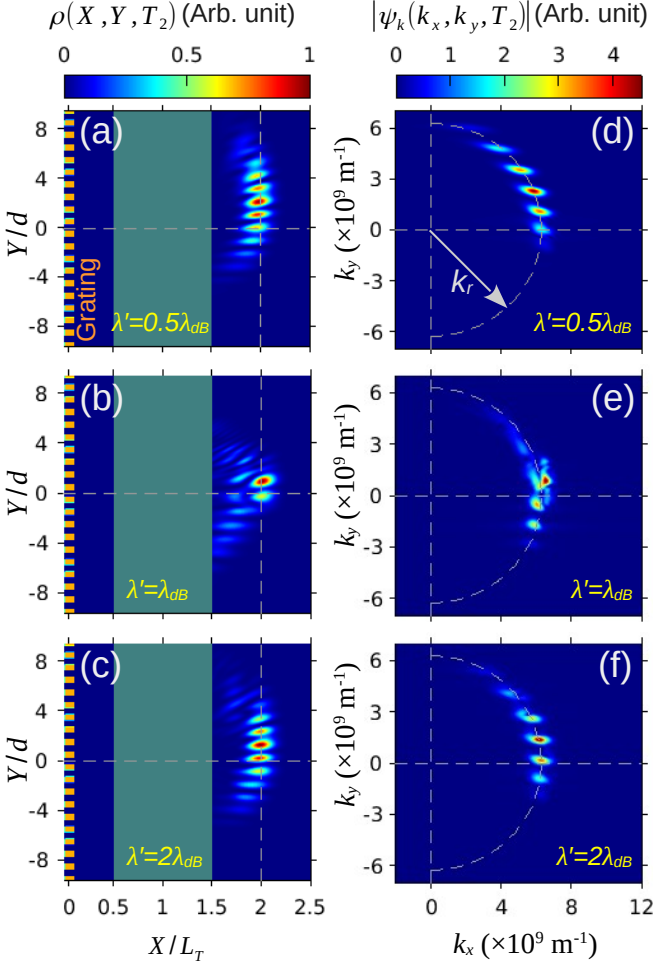


FIG. 11. Probability distribution $\rho(X, Y, T)$ of the diffracted wave packet at $T_2 = 5200$ for spatially modulated electrostatic fields with the length of modulation (a) $\lambda' = 0.5\lambda_{dB}$, (b) $\lambda' = \lambda_{dB}$, and (c) $\lambda' = 2\lambda_{dB}$. The electric field is employed in the transverse direction (along the y -axis). The distributions of the corresponding wave packets ($|\psi_k(k_x, k_y, T_2)|$) in the wave number space (k_x, k_y) are shown for (d) $\lambda' = 0.5\lambda_{dB}$, (e) $\lambda' = \lambda_{dB}$, and (f) $\lambda' = 2\lambda_{dB}$. Here, $k_r (= 6.28 \times 10^9 \text{ m}^{-1})$ is the wave number of the initial wave packet.

the direction of propagation ($\theta = 0^\circ$). This happens because, in this case, the electric field accelerates the diffracted wave packet associated with the particle, only in the axial direction (x -direction) while the transverse momentum of each peak remains unchanged. Hence, for $\theta = 0^\circ$, the transverse coherence is maintained, and consequently, the visibility increases.

C. Near-field diffraction in a spatially modulated electric field

A spatially modulated electrostatic field is employed in the region $L_T/2 \leq x \leq 3L_T/2$ to investigate its effect on the Talbot fringe. The electric field is taken as

$$\vec{E}(x, y) = \hat{y}E_0|\cos(k'x)|, \quad (13)$$

where $E_0 = 100 \text{ V/m}$ and the parameter $k' = 2\pi/\lambda'$ determines the degree of spatial modulation of the electric field along the x -direction. When the length of modulation λ' is comparable to λ_{dB} , it is expected that the spatial modulation in the electric field will influence the dynamics of the wave packet and hence, on the Talbot pattern, in addition to the fringe shift along the transverse direction that is brought about by E_0 alone. To study this effect, in our simulation, the values of λ' are taken as $0.5\lambda_{dB}$, λ_{dB} and $2\lambda_{dB}$.

Figs. 11(a)-(c) show the distribution of the probability density $\rho(X, Y, T_2)$ at $T_2 = 5200$ for $\lambda' = 0.5\lambda_{dB}$, λ_{dB} , and $2\lambda_{dB}$, respectively. The distributions of the corresponding wave packets in the wave number space are shown in Figs. 11(d)-(f). It can be noticed that for $\lambda' = 0.5\lambda_{dB}$ (see Fig. 11(a)), except the fringe shift along the y -axis, there seems to be no additional effect on the diffraction pattern, which is similar to the case of a uniform electric field E_0 employed along the y -axis (cf. Fig. 4(c)). This is also clear from the distribution of $|\psi_k(k_x, k_y, T_2)|$ as shown in Fig. 11(d), which indicates that the modulation in the electric field along x -direction has negligible influence on the wave packet when $\lambda' \leq 0.5\lambda_{dB}$.

The wave packet gets affected by the spatial modulation of the electric field when $\lambda' = \lambda_{dB}$, as shown in Fig. 11(b), where distortions in the diffraction pattern become visible. Moreover, the higher order peaks get overlapped each other, which becomes clear from the distribution of $|\psi_k(k_x, k_y, T_2)|$, as shown in Fig. 11(e). This happens because the wave packet, once diffracted by the grating, gets further diffracted by the spatially modulated potential barriers aligned along y -direction, which arises due to the spatially modulated electric field. As a result, distortions occur in the final diffraction pattern. As expected, this effect decreases with the increase in λ' beyond λ_{dB} , as shown in Fig. 11(c) for $\lambda' = 2\lambda_{dB}$, which is further confirmed from the distribution of $|\psi_k(k_x, k_y, T_2)|$, as shown in Fig. 11(f). Most interestingly, from the semi-circular distribution of $|\psi_k(k_x, k_y, T_2)|$ having a radius of $k_r (= 6.28 \times 10^9 \text{ m}^{-1})$, it is clear that the momentum of the diffracted wave packet is conserved in all the cases since the electrostatic field is applied in the transverse direction.

TABLE II. Values of the wave numbers (k_n^η) for different sidebands obtained from Eq. (15) and simulation.

n	Frequency (ω) (rad/s)	Sideband (η)	k_n^η ($\times 10^9 \text{ m}^{-1}$)	
			Theory (Eq. (15))	Simulation
4	$4\omega_0$	-2	3.74	3.71
		-1	5.16	5.17
		0	6.28	6.31
		1	7.20	7.23
		2	8.02	8.07
8	$8\omega_0$	-1	3.74	3.69
		0	6.28	6.30
		1	8.02	8.01
		2	9.46	9.51
12	$12\omega_0$	-1	2.38	2.41
		0	6.28	6.30
		1	8.52	8.50

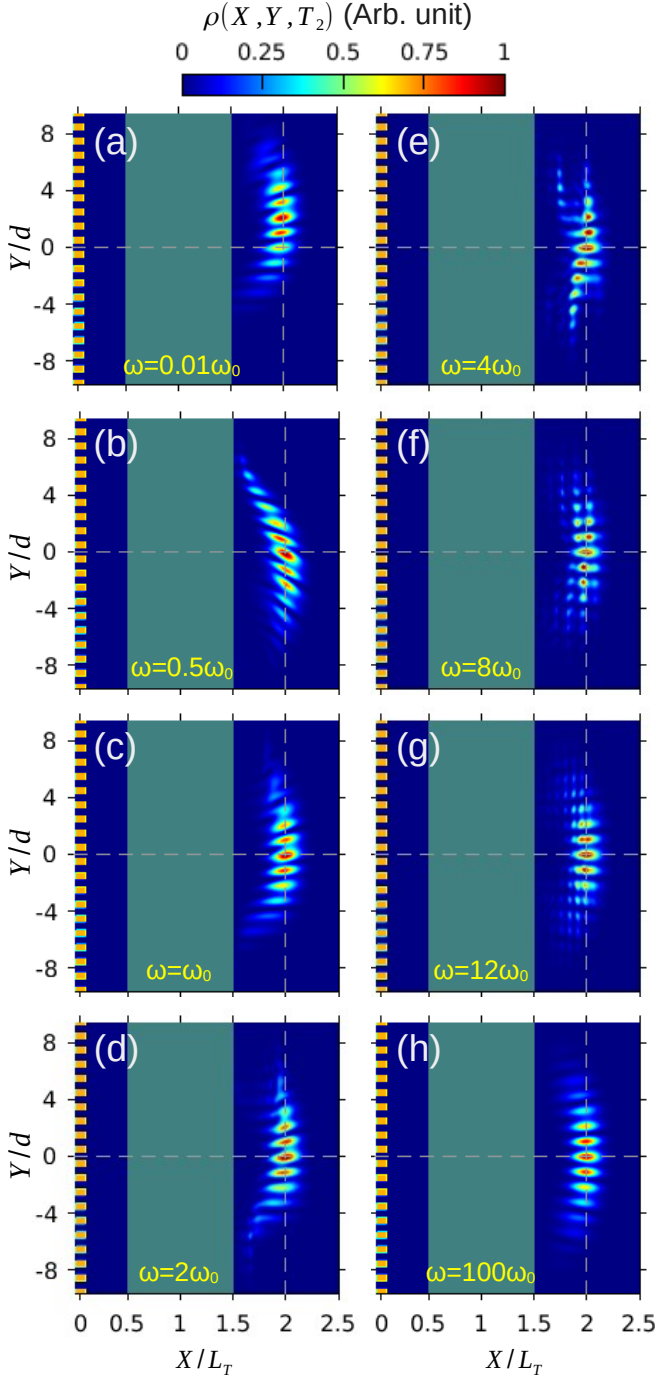


FIG. 12. Probability distribution $\rho(X, Y, T_2) = |\psi(X, Y, T_2)|^2$ of the diffracted wave packet after interacting with an oscillating electric field having amplitude $E_0 = 100$ V/m employed in the region $L_T/2 \leq x \leq 3L_T/2$ along the transverse direction ($\theta = 90^\circ$). The frequency of the oscillating electric fields are (a) $\omega = 0.01\omega_0$, (b) $\omega = 0.5\omega_0$, (c) $\omega = \omega_0$, (d) $\omega = 2\omega_0$, (e) $\omega = 4\omega_0$, (f) $\omega = 8\omega_0$, (g) $\omega = 12\omega_0$, and (h) $\omega = 100\omega_0$, where $\omega_0 = 2\pi/T_0$ and $T_0 (= L_T/v)$ is the time the wave packet takes to cross the electric field region. It can be seen that distortions in $\rho(X, Y, T_2)$ occurs at $\omega = 0.5\omega_0$ (panel (b)). With further increase in ω , sidebands started to appear, as shown in panel (d). The sidebands become visible at $\omega = 4\omega_0$ (panel (e)). Panel (h) shows that at higher frequencies, such as $\omega = 100\omega_0$, the sidebands disappear.

D. Near-field diffraction in a temporally modulated electric field

We next investigate the effect of a temporally modulated electric field on the diffraction pattern. The electric field is taken as

$$\vec{E}(x, y, t) = \hat{y}E_0 \cos(\omega t), \quad (14)$$

where $E_0 (= 100$ V/m) is the amplitude, and ω is the modulation frequency of the field applied in the transverse direction (y -axis) in the region $L_T/2 \leq x \leq 3L_T/2$. It is expected that the electric field will influence the dynamics of the diffracted wave packet when the value of ω is of the order of $\omega_0 (= 2\pi/T_0 \sim 39.5$ MHz), where $T_0 (= L_T/v)$ is the interaction time of the wave packet with the oscillating field and v is the velocity of the incident particle [77].

Figs. 12(a)-(h) show the probability distribution $\rho(X, Y, T_2)$ of the diffracted wave packet after interacting with the temporally modulated electric field for the frequencies ranging from $0.01\omega_0$ to $100\omega_0$. The corresponding distributions of $|\psi_k(k_x, k_y, T_2)|$ in the wave number space (k_x, k_y) are shown in Figs. 13(a)-(h). For $\omega \ll \omega_0$, no additional effects were observed, as shown in Fig. 12(a), except the fringe shift similar to the case of a uniform electric field (cf. Fig. 4(c)), due to the slower time variation of the field compared to the interaction time T_0 . Significant distortion occurs in $\rho(X, Y, T_2)$ at $\omega = 0.5\omega_0$ (Fig. 12(b)), which is also clear in the distribution of $|\psi_k(k_x, k_y, T_2)|$, as shown in Fig. 13(b). With further increase in ω , sidebands start to appear in the distribution, as shown in Figs. 13(c) and (d). It is observed that, unlike for the uniform field case, the fringe shift in the transverse direction becomes zero when ω is comparable to ω_0 or more, as shown in Fig. 12(c)-(h). This happens because the wave packet spends an approximately equal amount of time in the oppositely directed electric field of a complete oscillation throughout the interaction. At $\omega = 4\omega_0$, sidebands appear to appear in the diffracted wave packet, as shown in the Fig. 12(e) and Fig. 13(e). Sideband formation in matter waves optics has previously been studied for other systems, such as reflection of cold atoms from a vibrating surface [74, 77] and scattering of atoms by standing waves of light [78]. However, sideband formation in the Talbot pattern for charged particle matter waves using temporally modulated electric field is observed for the first time in this study. These sidebands appear due to the energy transfer from the oscillating field to the wave packet in an integer multiple of $\hbar\omega$. Therefore, energy of η^{th} band can be obtained as $E_\eta = E_{k_0} + \eta\hbar\omega$, where $\eta \in \mathbb{Z}$ [74, 79]. The upper bands are formed when $\eta > 0$, and for lower bands, $\eta < 0$. Therefore, the resulting momentum of the transmitted wave packet gets discretized for different bands, and the allowed wave numbers can be obtained as

$$k_n^\eta = \frac{1}{\hbar} \sqrt{2m(E_{k_0} + \eta\hbar\omega)}, \quad (15)$$

where $n = \omega/\omega_0$. However, it is clear that η should be such that $\eta \geq -E_{k_0}/\hbar\omega$. The values of the possible wave num-

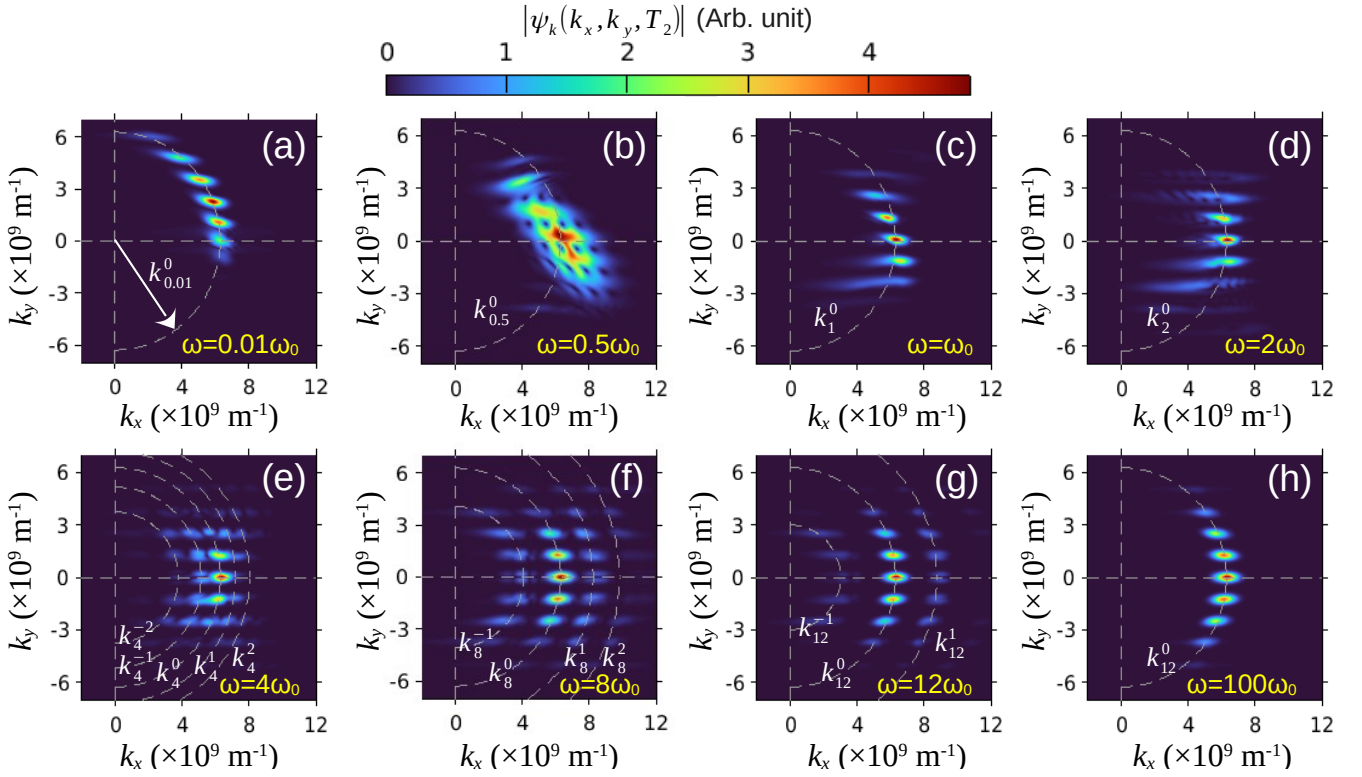


FIG. 13. Distribution of the diffracted wave packet $|\psi(k_x, k_y, T_2)|$ in the wave number space (k_x, k_y) after interacting with the oscillating electric field having a frequency (a) $\omega = 0.01\omega_0$, (b) $\omega = 0.5\omega_0$, (c) $\omega = \omega_0$, (d) $\omega = 2\omega_0$, (e) $\omega = 4\omega_0$, (f) $\omega = 8\omega_0$, (g) $\omega = 12\omega_0$, and (h) $\omega = 100\omega_0$. It can be noticed that when ω is of the order of ω_0 , sidebands start to appear due to the efficient energy transfer from the oscillating field to the wave packet in an integer (η) multiple of $\hbar\omega$. Positive values of η indicate upper band peaks, while negative values of η indicate lower band peaks. These sidebands are visible for $\omega = 4\omega_0$. The well-formed bands have a circular distribution in the wave number space having radius k_n^η , where $n = \omega/\omega_0$. These sidebands vanish when $\omega \ll \omega_0$ or $\omega \gg \omega_0$, which is clear from the panels (a) and (h).

bers k_n^η for different bands obtained from Eq. (15) and simulation are listed in Table II.

For $\omega = 4\omega_0$, several peaks in the upper bands (k_4^1, k_4^2 and k_4^3) and lower bands (k_4^{-1}, k_4^{-2}) including the central band (k_4^0) are observed, as shown in Fig. 13(e). From Fig. 13(e), it is clear that the positions of the peaks of different sidebands obtained from the simulation agree well with the predicted values of k_n^η obtained using Eq. (15). Further, an increase in ω causes the upper and lower bands to move far away from the central one with increasing and decreasing momentum, respectively, as shown in Figs. 13(f) and (g). This happens because the energy transfer ($\eta\hbar\omega$) becomes larger at higher frequencies. Moreover, it is observed that at higher frequencies ($\omega > 4\omega_0$), the number of peaks in the upper and lower bands decreases, as shown in Fig. 13(e)-(g). The sidebands completely disappear at $\omega = 100\omega_0$, as shown in Fig. 13(h). This is because the efficiency of energy transfer from the temporally modulated field to the wave packet decreases at higher frequencies. Interestingly, it is observed that the wave number (k_n^η) of the sidebands does not change with the amplitude E_0 of the electric field since the energy transfer depends only on ω . Instead, a decrease in E_0 causes a reduction in the amplitude of the sidebands. Therefore, the sidebands can be tuned by controlling the modulation frequency (ω) of the employed

electric field.

IV. CONCLUSION

Influence of (a) uniform, (b) spatially modulated, and (c) temporally modulated electric field (\vec{E}) on the near-field diffraction of protons by a nanostructured metallic grating are investigated. To obtain the diffraction pattern, time-domain simulations are performed for two-dimensional Gaussian wave packets by solving the time-dependent Schrödinger's equation using the generalized finite difference time domain (GFDTD-Q) method for quantum systems. The study reveals that:

(i) For a uniform electric field, the Talbot fringes get shifted along the transverse direction, and the amount of fringe shift depends upon E_0 and θ . Moreover, the Talbot fringe is sensitive ($(SF)_{E_0} = 1.1\%$ and $(SF)_\theta = 3.37\%$) even to a small ΔE_0 ($= 0.1$ V/m) and $\Delta\theta$ ($= 0.1^\circ$). The resolution of ΔE_0 and $\Delta\theta$ can be improved further by extending the region of interaction of the diffracted wave packet with \vec{E} beyond L_T .

(ii) It is found that the applied uniform electric field can tune the Talbot fringe visibility.

(iii) For a spatially modulated electric field, significant dis-

tortions are observed in the Talbot patterns when the length of modulation (λ') is equal to λ_{dB} . The distortions occur because the wave packet gets further diffracted by the potential barriers arising from the spatial modulation of \vec{E} .

(iv) For a temporally modulated electric field, multiple sidebands are observed for the first time in the Talbot pattern when the frequency of oscillation is of the order of $\omega_0 (= 2\pi/T_0)$, where T_0 is the interaction time. The sidebands have discrete momentum states that appear due to an efficient energy transfer from the oscillating electric field to the wave packet at an integer multiple of $\hbar\omega$. Therefore, the momentum states of the sidebands, which are found to be independent of E_0 , can be controlled by tuning ω .

The findings of this research will be helpful in various emerging applications of quantum technologies. The electric field sensitivity of the Talbot pattern of protons can be used to

develop sensors to accurately measure small electric fields and to align the matter wave optical setup precisely. The electric field-dependent fringe visibility can be used in high-precision and controlled metrology. Finally, sidebands in the Talbot fringe can be used as a precise tool for momentum splitter in matter wave interferometry.

ACKNOWLEDGMENTS

We gratefully acknowledge the financial support from the funding agency SERB (Department of Science and Technology), Government of India, Grant No. CRG/2022/000112. The simulations were performed at the High Performance Computing facility (HPC2013) at IIT Kanpur.

-
- [1] H.F. Talbot Esq. F.R.S., “Lxxvi. facts relating to optical science. no. iv,” *The London, Edinburgh, and Dublin Philosophical Magazine and Journal of Science* **9**, 401–407 (1836).
 - [2] Yong Zhang, Jianming Wen, S. N. Zhu, and Min Xiao, “Non-linear talbot effect,” *Phys. Rev. Lett.* **104**, 183901 (2010).
 - [3] Hugues Guillet de Chatellus, Luis Romero Cortés, Antonin Deville, Mohamed Seghilani, and José Azaña, “Diffraction-induced bidimensional talbot self-imaging with full independent period control,” *Phys. Rev. Lett.* **118**, 133903 (2017).
 - [4] Layton A Hall, Murat Yessenov, Sergey A Ponomarenko, and Ayman F Abouraddy, “The space–time talbot effect,” *APL Photonics* **6**, 056105 (2021).
 - [5] Damien Bigourd, Béatrice Chatel, Wolfgang P. Schleich, and Bertrand Girard, “Factorization of numbers with the temporal talbot effect: Optical implementation by a sequence of shaped ultrashort pulses,” *Phys. Rev. Lett.* **100**, 030202 (2008).
 - [6] José S. Rodrigues, Caio V. C. Mendes, Eduardo J. S. Fonseca, and Alcenísio J. Jesus-Silva, “Talbot effect in optical lattices with topological charge,” *Opt. Lett.* **42**, 3944–3947 (2017).
 - [7] Madhuri Thakur, Cho Jui Tay, and Chenggen Quan, “Surface profiling of a transparent object by use of phase-shifting talbot interferometry,” *Appl. Opt.* **44**, 2541–2545 (2005).
 - [8] Mahendra P. Kothiyal and Rajpal S. Sirohi, “Improved collimation testing using talbot interferometry,” *Appl. Opt.* **26**, 4056–4057 (1987).
 - [9] Shashi Prakash, Sanjay Upadhyay, and Chandra Shakher, “Real time out-of-plane vibration measurement/monitoring using talbot interferometry,” *Optics and Lasers in Engineering* **33**, 251–259 (2000).
 - [10] H. Hamam and J. L. de Bougrenet de la Tocnaye, “Efficient fresnel-transform algorithm based on fractional fresnel diffraction,” *J. Opt. Soc. Am. A* **12**, 1920–1931 (1995).
 - [11] Mitsuo Takeda and Seiji Kobayashi, “Lateral aberration measurements with a digital talbotinterferometer,” *Appl. Opt.* **23**, 1760–1764 (1984).
 - [12] Yoshiaki Nakano and Kazumi Murata, “Talbot interferometry for measuring the focal length of a lens,” *Appl. Opt.* **24**, 3162–3166 (1985).
 - [13] Yoshiaki Nakano, “Measurements of the small tilt-angle variation of an object surface using moire interferometry and digital image processing,” *Appl. Opt.* **26**, 3911–3914 (1987).
 - [14] Thanarwut Photia, Wipawee Temnuch, Sorakrai Srisuphaphon, Nuttanan Tanasanchai, Waranont Anukool, Kunaree Wongrath, Pachara Manit, Surasak Chiangga, and Sarayut Deachapunya, “High-precision grating period measurement,” *Appl. Opt.* **58**, 270–273 (2019).
 - [15] Chandra Shakher and A. J. Pramila Daniel, “Talbot interferometer with circular gratings for the measurement of temperature in axisymmetric gaseous flames,” *Appl. Opt.* **33**, 6068–6072 (1994).
 - [16] Pituk Panthong, Sorakrai Srisuphaphon, Surasak Chiangga, and Sarayut Deachapunya, “High-contrast optical vortex detection using the talbot effect,” *Appl. Opt.* **57**, 1657–1661 (2018).
 - [17] Ningren Han, Gavin N. West, Amir H. Atabaki, David Burghoff, and Rajeev J. Ram, “Compact and high-precision wavemeters using the talbot effect and signal processing,” *Opt. Lett.* **44**, 4187–4190 (2019).
 - [18] C. J. Davisson and L. H. Germer, “Reflection of electrons by a crystal of nickel,” *PNAS* **14**, 317–322 (1928).
 - [19] L. Marton, J. Arol Simpson, and J. A. Suddeth, “Electron beam interferometer,” *Phys. Rev.* **90**, 490–491 (1953).
 - [20] Ernst M. Rasel, Markus K. Oberthaler, Herman Batelaan, Jörg Schmiedmayer, and Anton Zeilinger, “Atom wave interferometry with diffraction gratings of light,” *Phys. Rev. Lett.* **75**, 2633–2637 (1995).
 - [21] Pippa Storey, Matthew Collett, and Daniel Walls, “Measurement-induced diffraction and interference of atoms,” *Phys. Rev. Lett.* **68**, 472–475 (1992).
 - [22] Phillip L. Gould, George A. Ruff, and David E. Pritchard, “Diffraction of atoms by light: The near-resonant kapitza-dirac effect,” *Phys. Rev. Lett.* **56**, 827–830 (1986).
 - [23] D. W. Keith, M. L. Schattenburg, Henry I. Smith, and D. E. Pritchard, “Diffraction of atoms by a transmission grating,” *Phys. Rev. Lett.* **61**, 1580–1583 (1988).
 - [24] G Gronniger, B Barwick, and H Batelaan, “A three-grating electron interferometer,” *New J. Phys.* **8**, 224 (2006).
 - [25] Jorge A. Salas, Kalman Varga, Jia-An Yan, and Kirk H. Bevan, “Electron talbot effect on graphene,” *Phys. Rev. B* **93**, 104305 (2016).
 - [26] S. Sala, A. Ariga, A. Ereditato, R. Ferragut, M. Giammarchi, M. Leone, C. Pistillo, and P. Scamporrì, “First demonstration of antimatter wave interferometry,” *Sci. Adv.* **5**, eaav7610 (2019).

- [27] S. Nowak, Ch. Kurtsiefer, T. Pfau, and C. David, “High-order talbot fringes for atomic matter waves,” *Opt. Lett.* **22**, 1430–1432 (1997).
- [28] Michael S. Chapman, Christopher R. Ekstrom, Troy D. Hammond, Jörg Schmiedmayer, Bridget E. Tannian, Stefan Wehinger, and David E. Pritchard, “Near-field imaging of atom diffraction gratings: The atomic talbot effect,” *Phys. Rev. A* **51**, R14–R17 (1995).
- [29] Manfred J Mark, Elmar Haller, Johann G Danzl, Katharina Lauber, Mattias Gustavsson, and Hanns-Christoph Nägerl, “Demonstration of the temporal matter-wave talbot effect for trapped matter waves,” *New J. Phys.* **13**, 085008 (2011).
- [30] Simon R Müller, Patrick Nedelec, and Markus K Oberthaler, “From classical xenon fringes to hydrogen interferometry,” *New J. Phys.* **22**, 073060 (2020).
- [31] C Kohstall, S Riedl, E R Sánchez Guajardo, L A Sidorenkov, J Hecker Denschlag, and R Grimm, “Observation of interference between two molecular bose–einstein condensates,” *New J. Phys.* **13**, 065027 (2011).
- [32] Lucia Hackermüller, Klaus Hornberger, Stefan Gerlich, Michael Gring, Hendrik Ulbricht, and Markus Arndt, “Optical polarizabilities of large molecules measured in near-field interferometry,” *Appl. Phys. B* **89**, 469–473 (2007).
- [33] Martin Berninger, André Stefanov, Sarayut Deachapunya, and Markus Arndt, “Polarizability measurements of a molecule via a near-field matter-wave interferometer,” *Phys. Rev. A* **76**, 013607 (2007).
- [34] Stefan Gerlich, Lucia Hackermüller, Klaus Hornberger, Alexander Stibor, Hendrik Ulbricht, Michael Gring, Fabienne Goldfarb, Tim Savas, Marcel Müri, Marcel Mayor, *et al.*, “A kapitza–dirac–talbot–lau interferometer for highly polarizable molecules,” *Nat. Phys.* **3**, 711–715 (2007).
- [35] Björn Brezger, Lucia Hackermüller, Stefan Uttenthaler, Julia Petschinka, Markus Arndt, and Anton Zeilinger, “Matter-wave interferometer for large molecules,” *Phys. Rev. Lett.* **88**, 100404 (2002).
- [36] Sandra Eibenberger, Stefan Gerlich, Markus Arndt, Jens Tüxen, and Marcel Mayor, “Electric moments in molecule interferometry,” *New J. Phys.* **13**, 043033 (2011).
- [37] James Bateman, Stefan Nimmrichter, Klaus Hornberger, and Hendrik Ulbricht, “Near-field interferometry of a free-falling nanoparticle from a point-like source,” *Nat. Commun.* **5**, 4788 (2014).
- [38] Sandra Eibenberger, Stefan Gerlich, Markus Arndt, Marcel Mayor, and Jens Tüxen, “Matter-wave interference of particles selected from a molecular library with masses exceeding 10000 amu,” *Phys. Chem. Chem. Phys.* **15**, 14696–14700 (2013).
- [39] Björn Brezger, Markus Arndt, and Anton Zeilinger, “Concepts for near-field interferometers with large molecules,” *J. Opt. B: Quantum Semiclass. Opt.* **5**, S82 (2003).
- [40] Stefan Nimmrichter and Klaus Hornberger, “Theory of near-field matter-wave interference beyond the eikonal approximation,” *Phys. Rev. A* **78**, 023612 (2008).
- [41] S K Lee, M S Kim, C Szewc, and H Ulbricht, “Phase-space tomography of matter-wave diffraction in the talbot regime,” *New J. Phys.* **14**, 045001 (2012).
- [42] S Srisuphaphon, W Temnuch, S Buathong, and S Deachapunya, “Matter-wave interferometry from near-field to far-field diffraction,” *J. Phys.: Conf. Ser.* **1380**, 012083 (2019).
- [43] C Artyooha, S Deachapunya, B Krunavakarn, N Kheo-maingam, and S Srisuphaphon, “A study of matter-wave diffraction for particle in the near field regime under the influence of a uniform electric field,” *J. Phys.: Conf. Ser.* **1144**, 012053 (2018).
- [44] Farhan Saif, “Talbot effect with matter waves,” *Laser Phys.* **22**, 1874–1878 (2012).
- [45] Ana García-Cabrera, Carlos Hernández-García, and Luis Plaja, “Ultrafast sub-nanometer matter-wave temporal talbot effect,” *New J. Phys.* **23**, 093011 (2021).
- [46] P Kazemi, S Chaturvedi, I Marzoli, R F O’Connell, and W P Schleich, “Quantum carpets: a tool to observe decoherence,” *New J. Phys.* **15**, 013052 (2013).
- [47] Simone Sala, Fabrizio Castelli, Marco Giammarchi, Stefano Siccardi, and Stefano Olivares, “Matter-wave interferometry: towards antimatter interferometers,” *J. Phys. B: At. Mol. Opt. Phys.* **48**, 195002 (2015).
- [48] Michael Gring, Stefan Gerlich, Sandra Eibenberger, Stefan Nimmrichter, Tarik Berrada, Markus Arndt, Hendrik Ulbricht, Klaus Hornberger, Marcel Müri, Marcel Mayor, Marcus Böckmann, and Nikos L. Doltsinis, “Influence of conformational molecular dynamics on matter wave interferometry,” *Phys. Rev. A* **81**, 031604 (2010).
- [49] Thomas Juffmann, Hendrik Ulbricht, and Markus Arndt, “Experimental methods of molecular matter-wave optics,” *Rep. Prog. Phys.* **76**, 086402 (2013).
- [50] S Stauss, H Muneoka, N Ebato, F Oshima, D Z Pai, and K Terashima, “Self-organized pattern formation in helium dielectric barrier discharge cryoplasmas,” *Plasma Sources Sci. Technol.* **22**, 025021 (2013).
- [51] Yuri Noma, Jai Hyuk Choi, Hitoshi Muneoka, and Kazuo Terashima, “Electron density and temperature of gas-temperature-dependent cryoplasma jet,” *J. Appl. Phys.* **109**, 053303 (2011).
- [52] Lord Rayleigh F.R.S., “Xxv. on copying diffraction-gratings, and on some phenomena connected therewith,” *The London, Edinburgh, and Dublin Philosophical Magazine and Journal of Science* **11**, 196–205 (1881).
- [53] Mahboubeh Ghalandari and M Solaimani, “Fractional young double-slit numerical experiment with gaussian wavepackets,” *Scientific Reports* **10**, 19458 (2020).
- [54] Sushanta Barman and Sudeep Bhattacharjee, “Time-domain simulation of charged particle diffraction by an electrostatically biased grating: Transmission tunability and shaping of the quantum point contact for protons,” *J. Appl. Phys.* **132**, 034401 (2022).
- [55] G. Rojas-Lorenzo, J. Rubayo-Soneira, S. Miret-Artés, and E. Pollak, “Quantum threshold reflection of he-atom beams from rough surfaces,” *Phys. Rev. A* **101**, 022506 (2020).
- [56] Salvador Miret-Artés and Eli Pollak, “Scattering of he atoms from a microstructured grating: Quantum reflection probabilities and diffraction patterns,” *J. Phys. Chem. Lett.* **8**, 1009–1013 (2017).
- [57] Alejandro Castellanos-Jaramillo and Arnulfo Castellanos-Moreno, “Spatial and temporal description of electron diffraction through a double slit at the nanometer scale,” *Eur. J. Phys.* **39**, 065403 (2018).
- [58] Brett Barwick, Glen Gronniger, Lu Yuan, Sy-Hwang Liou, and Herman Batelaan, “A measurement of electron-wall interactions using transmission diffraction from nanofabricated gratings,” *J. Appl. Phys.* **100**, 074322 (2006).
- [59] Frederick Ira Moxley, Tim Byrnes, Fumitaka Fujiwara, and Weizhong Dai, “A generalized finite-difference time-domain quantum method for the n-body interacting hamiltonian,” *Comput. Phys. Commun.* **183**, 2434–2440 (2012).
- [60] Frederick Ira Moxley, David T. Chuss, and Weizhong Dai, “A generalized finite-difference time-domain scheme for solving nonlinear schrödinger equations,” *Comput. Phys. Commun.* **184**, 1834–1841 (2013).

- [61] Pieter Decler, Arne Van Londersele, Hendrik Rogier, and Dries Vande Ginste, “An alternating-direction hybrid implicit-explicit finite-difference time-domain method for the schrödinger equation,” *J. Comput. Appl. Math.* **403**, 113881 (2022).
- [62] Joshua P. Wilson, “Generalized finite-difference time-domain method with absorbing boundary conditions for solving the nonlinear schrödinger equation on a gpu,” *Comput. Phys. Commun.* **235**, 279–292 (2019).
- [63] Frederick Ira Moxley, Tim Byrnes, Baoling Ma, Yun Yan, and Weizhong Dai, “A g-fdtd scheme for solving multi-dimensional open dissipative gross–pitaevskii equations,” *J. Comput. Phys.* **282**, 303–316 (2015).
- [64] I Wayan Sudiarta and D J Wallace Geldart, “Solving the schrödinger equation using the finite difference time domain method,” *J. Phys. A: Math. Theor.* **40**, 1885 (2007).
- [65] Antonio Soriano, Enrique A Navarro, Jorge A Porti, and Vicente Such, “Analysis of the finite difference time domain technique to solve the schrödinger equation for quantum devices,” *J. Appl. Phys.* **95**, 8011–8018 (2004).
- [66] Dennis M Sullivan and DS Citrin, “Determination of the eigenfunctions of arbitrary nanostructures using time domain simulation,” *J. Appl. Phys.* **91**, 3219–3226 (2002).
- [67] Huali Duan, Wenxiao Fang, Wen-Yan Yin, Erping Li, and Wenchao Chen, “Computational investigation of nanoscale semiconductor devices and optoelectronic devices from the electromagnetics and quantum perspectives by the finite difference time domain method,” *Prog. Electromagn. Res.* **170** (2021).
- [68] Pieter Decler, Arne Van Londersele, Hendrik Rogier, and Dries Vande Ginste, “Nonuniform and higher-order fdtd methods for the schrödinger equation,” *J. Comput. Appl. Math.* **381**, 113023 (2021).
- [69] Tara Ghafouri, Zohreh Golshan Bafghi, Nima Nouri, and Negin Manavizadeh, “Numerical solution of the schrödinger equation in nanoscale side-contacted fed applying the finite-difference method,” *Results Phys.* **19**, 103502 (2020).
- [70] Nahid Talebi and Iva Březinová, “Exchange-mediated mutual correlations and dephasing in free-electrons and light interactions,” *New J. Phys.* **23**, 063066 (2021).
- [71] Nahid Talebi, “Electron-light interactions beyond the adiabatic approximation: recoil engineering and spectral interferometry,” *Adv. Phys.: X* **3**, 1499438 (2018).
- [72] Nahid Talebi, “Schrödinger electrons interacting with optical gratings: quantum mechanical study of the inverse smith–purcell effect,” *New J. Phys.* **18**, 123006 (2016).
- [73] Dennis M Sullivan and DS Citrin, “Time-domain simulation of a universal quantum gate,” *J. Appl. Phys.* **96**, 1540–1546 (2004).
- [74] Benedikt Herwerth, Maarten DeKieviet, Javier Madroñero, and Sandro Wimberger, “Quantum reflection from an oscillating surface,” *J. Phys. B: At. Mol. Opt. Phys.* **46**, 141002 (2013).
- [75] Klaus Hornberger, Stefan Gerlich, Philipp Haslinger, Stefan Nimmrichter, and Markus Arndt, “Colloquium: Quantum interference of clusters and molecules,” *Rev. Mod. Phys.* **84**, 157–173 (2012).
- [76] Xiangyuan Wang, Yixuan Meng, Wei-Wei Huang, Linlin Li, Zhiwei Zhu, and LiMin Zhu, “Design, modeling, and test of a normal-stressed electromagnetic actuated compliant nanopositioning stage,” *Mechanical Systems and Signal Processing* **185**, 109753 (2023).
- [77] A Steane, P Szriftgiser, P Desbiolles, and J Dalibard, “Phase modulation of atomic de broglie waves,” *Phys. Rev. Lett.* **74**, 4972 (1995).
- [78] S Bernet, R Abfalterer, C Keller, MK Oberthaler, J Schmiedmayer, and A Zeilinger, “Matter waves in time-modulated complex light potentials,” *Phys. Rev. A* **62**, 023606 (2000).
- [79] Tommy A Byrd, Megan K Ivory, Andrew J Pyle, Seth Aubin, Kevin A Mitchell, John B Delos, and Kunal K Das, “Scattering by an oscillating barrier: Quantum, classical, and semiclassical comparison,” *Phys. Rev. A* **86**, 013622 (2012).